Topological Hall effect in the Shastry-Sutherland lattice

Munir Shahzad[1], Nyayabanta Swain[2], and Pinaki Sengupta[2]

[1]*Department of Physics and Physical Oceanography, Memorial University of Newfoundland,*
St. John's, Newfoundland & Labrador, Canada A1B 3X7

[2]*School of Physical and Mathematical Sciences, Nanyang Technological University, 21 Nanyang Link, 637371 Singapore*

We study the classical Heisenberg model on the geometrically frustrated Shastry-Sutherland (SS) lattice with additional Dzyaloshinskii-Moriya (DM) interaction in the presence of an external magnetic field. We show that several noncollinear and noncoplanar magnetic phases, such as the flux, all-in/all-out, 3-in–1-out/3-out–1-in, and canted-flux phases are stabilized over wide ranges of parameters in the presence of the DM interaction. We discuss the role of DM interaction in stabilizing these complex magnetic phases. When coupled to these noncoplanar magnetic phases, itinerant electrons experience a finite Berry phase, which manifests in the form of topological Hall effect, whereby a nonzero transverse conductivity is observed even in the absence of a magnetic field. We study this anomalous magnetotransport by calculating the electron band structure and transverse conductivity for a wide range of parameter values, and demonstrate the existence of topological Hall effect in the SS lattice. We explore the role of the strength of itinerant electron-local moment coupling on electron transport and show that the topological Hall features evolve significantly from strong to intermediate values of the coupling strength, and are accompanied by the appearance of a finite spin Hall conductivity.

I. INTRODUCTION

The interplay of charge and spin degrees of freedom manifests in novel phases in strongly correlated electron systems [1–4]. One of the basic models that describes this interplay is the Kondo lattice model or the double-exchange (DE) model, in which localized magnetic moments are coupled to itinerant electrons [5–9]. In these systems the conduction electrons and localized spins affect each other in a self-consistent way. On the one hand, the mobile electrons mediate effective interactions between the localized spins, and dictate the magnetic behavior. On the other hand, the scattering of the mobile electrons from these localized moments decides the resulting electronic and transport properties of the system. This interplay becomes more interesting when the localized moments are arranged on a geometrically frustrated lattice [10–13]. In these frustrated systems, the ground state has a large degeneracy, leaving them strongly susceptible to even small perturbations like longer-range exchange interactions mediated by conduction electrons coupled to the localized moments. In some cases, the resulting effect of the spin-charge coupling leads to unconventional magnetic phases [14–18].

Among these phases, some of the most interesting are those with noncoplanar spin orderings, with nonzero scalar spin chirality [19–21]. The chiral nature of these states breaks both the parity and time-reversal symmetries. When an electron moves through a background of noncoplanar spin texture, it picks up a Berry phase, which gives rise to many interesting transport phenomena such as the geometric or topological Hall effect (THE) and unconventional magnetoresistive behavior

[14,22–24]. In THE, a transverse Hall current is observed even in the absence of any external applied magnetic field, driven solely by the cumulative Berry phase acquired by the electrons. The acquired Berry phase is equivalent to the coupling of electron orbital moment to a fictitious magnetic field.

THE has been observed in the ferromagnetic pyrocholre compounds $Pr_2Ir_2O_7$ and $Nd_2Mo_2O_7$ [14,25–27]. The chiral spin ordering has been studied theoretically in the context of Kondo lattice model on frustrated lattices such as triangular [28,29], kagome [21,30–33], pyrocholre [34], face-centered-cubic lattice [35], and checkerboard lattice [36]. Our plan is to extend this study to the geometrically frustrated Shastry-Sutherland (SS) lattice, which is a prototypical model of several materials like the rare-earth tetraborides [37–42]. These materials have rare-earth elements with large magnetic moments that can be treated as classical spins. This, in turn, renders the theoretical modeling of such systems more tractable. For classical spins, the Kondo lattice and double-exchange models can be mapped on to one another, as the eigenstates corresponding to opposite signs of the Kondo coupling are related by a global gauge transformation.

The SS lattice has several competing interactions in play owing to its unique lattice symmetry. The competition between the axial and diagonal exchange interactions usually results in a collinear or coplanar ordered phase [43–45]. However, a rich variety of phases, including noncoplanar phases, are expected when the symmetry-allowed Dzyaloshinskii-Moriya (DM) interaction is taken into account. Further, the use of an external Zeeman field enhances the possibility of having noncoplanar phases significantly. Previously, we have shown that the Kondo lattice model on the SS lattice exhibits

noncoplanar and noncollinear ground states over a wide range of parameters [46–48]. In this work, we aim to thoroughly study the effect of all the competing interactions in stabilizing the noncoplanar phases and investigate the transport properties of itinerant electrons on this lattice. The ability to realize multiple noncollinear and noncoplanar magnetic orderings by tuning different interactions for realistic values of model parameters make the SS lattice an ideal case for studying THE.

In this work, we demonstrate that multiple noncollinear and noncoplanar magnetic ground-state phases are stabilized in the SS lattice for different ranges of Hamiltonian parameters. The behavior of itinerant electrons is significantly modified by the coupling to the underlying spin textures. In particular, for noncoplanar magnetic orderings, this is manifested in the form of finite THE.

This paper is organized as follows. Following the Introduction in Sec. I, we discuss the models used in this study in Sec. II. In Sec. III we describe the method and the observables that we calculate to characterize the magnetic and the transport properties. We present the results of our work in Sec. IV, followed by the summary in Sec. V.

II. MODEL

We study the Hamiltonian

$$\hat{\mathcal{H}}^c = \sum_{\langle ij \rangle} J_{ij} \mathbf{S}_i \cdot \mathbf{S}_j + \sum_{\langle ij \rangle} \mathbf{D}_{ij} \cdot \mathbf{S}_i \times \mathbf{S}_j - B \sum_i S_i^z \quad (1)$$

on the SS lattice, where $\langle ij \rangle$ refers to nearest-neighbor axial bonds on each plaquette, and next-nearest-neighbor diagonal bonds on alternate plaquettes. The first term represents the Heisenberg exchange interaction, with $J_{ij} = J$ (J') denoting the strength of antiferromagnetic exchange on the axial (diagonal) bonds. The second term is the antisymmetric DM interaction with $\mathbf{D}_{ij}$ representing the DM vectors on SS bonds. The exact values and directions of these vectors are determined by the crystal structure, subject to the Moriya rules and the constraints imposed by the geometry of the lattice. In Fig. 1, the unit cell of the SS lattice together with the choice of all DM vectors on each bond is shown. We parametrize the DM vectors via their parallel ($D_{\parallel,s}$, $D_{\parallel,ns}$, D') and perpendicular ($D_\perp$) components. Further details on different components of the DM vectors are described in Fig. 1. The last term is the Zeeman coupling between localized spins and an external applied magnetic field.

We treat the localized spins as classical vectors (true for f-electron systems with large magnetic moments) with unit length ($|\mathbf{S}_i| = 1$). We use the spherical polar coordinates $\mathbf{S}_i = (\sin\theta_i \cos\phi_i, \sin\theta_i \sin\phi_i, \cos\theta_i)$ to denote the state of the localized spin. Henceforth, interactions on the diagonal bonds are represented with prime parameters while those on axial bonds with unprimed ones.

In order to study transport properties of itinerant electrons coupled to localized spin textures, we use the Kondo lattice model

$$\hat{\mathcal{H}}^e = -\sum_{\langle ij \rangle, \sigma} t_{ij}(c_{i,\sigma}^\dagger c_{j,\sigma} + \text{H.c.}) + J_K \sum_i \mathbf{S}_i \cdot \mathbf{s}_i, \quad (2)$$

where t_{ij} represents the hopping matrix elements of conduction electrons on the SS lattice bonds, and $J_K > 0$ is
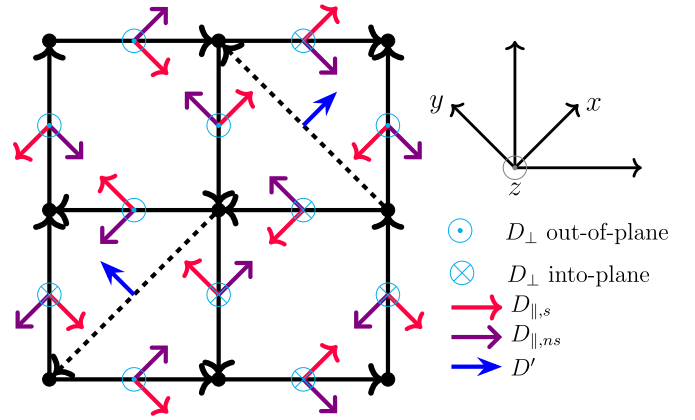
FIG. 1. The geometry of the SS lattice used in our study. Solid black lines represent the axial bonds while dotted black lines represent the diagonal bonds on alternate plaquette. The direction of the arrows on these bonds indicates the order of cross product $\mathbf{S}_i \times \mathbf{S}_j$ in DM term for these bonds. The in-plane component of DM vector on axial bonds is divided into staggered $D_{\parallel,s}$ and nonstaggered $D_{\parallel,ns}$ components, and represented by red and purple arrows, respectively. The in-plane component of DM vector on diagonal bonds D' is indicated by blue arrows. The perpendicular component of DM vector $D_\perp$ on axial bonds has out-of-plane and into-plane components. The directions of all these DM vectors are obtained using Moriya rules and crystal structure of the SS lattice.

the coupling strength of on-site Kondo term between classical spin $\mathbf{S}_i$ and the spin of itinerant electron $\mathbf{s}_i = c_{i\alpha}^\dagger \sigma^{\alpha\beta} c_{i\beta}$. $J_K/t \neq 0$ lifts the spin degeneracy of conduction electron states. In the limit of $J_K \gg t$, the electron bands form two blocks separated by a gap $\sim J_K$ corresponding to electron spins aligned parallel and antiparallel to the localized moments, with the spin-antiparallel states occupying the lower-energy bands compared to the spin-parallel states. In this limit, Hamiltonian (2) reduces to an effective tight-binding model [49] for the lower energy bands, given by

$$\hat{\mathcal{H}}_e = -\sum_{\langle i,j \rangle, \sigma} t_{ij}^{\text{eff}}(d_i^\dagger d_j + \text{H.c.}), \quad (3)$$

where

$$t_{ij}^{\text{eff}} = t_{ij} e^{ia_{ij}} \cos\frac{\theta_{ij}}{2} \quad (4)$$

is the effective hopping matrix elements for the spin-parallel electrons between sites i and j. The phase factor, related to spin chirality, is calculated as

$$a_{ij} = \arctan \frac{-\sin(\phi_i - \phi_j)}{\cos(\phi_i - \phi_j) + \cot\frac{\theta_i}{2}\cot\frac{\theta_j}{2}} \quad (5)$$

and θ_{ij} is the angle difference between the localized spins $\mathbf{S}_i$ and $\mathbf{S}_j$:

$$\cos\theta_{ij} = \cos\theta_i \cos\theta_j + \sin\theta_i \sin\theta_j \cos(\phi_i - \phi_j). \quad (6)$$

III. METHOD AND OBSERVABLES

To investigate the model in (1), we use a Markov chain Monte Carlo (MC) to perform an importance sampling of the spin configurations, based on the Metropolis algorithm.

The simulations are performed on lattices of dimension $L \times L$ with $L = 16$–48 over a wide range of Hamiltonian parameters. We use a simulated annealing procedure to prevent the freezing of the localized moments which may happen at low temperatures. In this approach, we start the simulations with a random spin configuration at a high temperature ($T \approx J$), and equilibrate the system at this temperature. Next, we decrease the temperature by ΔT and use the equilibrated spin configuration from previous T as an initial configuration for equilibration at the new temperature. We repeat this process until we reach $T = 0.001J$, where measurements are made to calculate the thermal averages of the physical observables. 100 000 MC steps are used at each T value as equilibration steps and further 50 000 MC steps are used to perform the measurements of the observables. We carried out the annealing procedure from a sufficiently high temperature so that the system can explore the whole phase space instead of getting stuck at a local minimum. Also, our lowest temperature in the simulation is lower than the finite-size gaps in the systems, thereby leading us to believe the calculated physical quantities with appropriate finite-size scaling yields an accurate estimate for the actual ground-state values.

In order to identify the magnetic order of localized spins, we calculate the static spin structure factor given by the Fourier transform of spin-spin correlation function

$$S(\mathbf{Q}) = \frac{1}{N^2} \sum_{i,j} \langle \mathbf{S}_i \cdot \mathbf{S}_j \rangle \exp[i\mathbf{Q} \cdot \mathbf{r}_{ij}], \tag{7}$$

where $\mathbf{r}_{ij} = \mathbf{r}_j - \mathbf{r}_i$ denotes the position vector from the ith to jth site, and $\langle \cdot \rangle$ represents the average over different MC configurations. Further, to distinguish between the coplanar and noncoplanar magnetic orders, we calculate scalar spin chirality as a measure of noncoplanarity of spin textures. On a triangular plaquette, the scalar spin chirality is defined as

$$\chi_\triangle = \mathbf{S}_i \cdot (\mathbf{S}_j \times \mathbf{S}_k). \tag{8}$$

The total chirality χ is calculated by $\chi = \frac{1}{N_u} \sum_\triangle \chi_\triangle$, where N_u is the number of SS unit cells. For collinear order (ferromagnetic and antiferromagnetic) and coplanar order (such as flux states), $\chi = 0$, whereas noncoplanar magnetic ordered phases such as canted-flux, all-in/all-out and 3-in–1-out/3-out–1-in phases are characterized by nonzero values of χ.

We use the Kubo formula to calculate the electronic transport on the magnetic ordered backgrounds on the SS lattice. In the limit $J_K/t \to \infty$, we can use the translational invariance of the effective tight-binding Hamiltonian (3) to calculate the momentum space Hamiltonian and obtain the energy spectrum of itinerant electrons moving on a background ordered phase. We calculate the transverse conductivity in $\mathbf{k}$-space as

$$\sigma_{xy} = \frac{ie^2\hbar}{N} \sum_{m,n\neq m,\mathbf{k}} [f(\mathcal{E}_{m\mathbf{k}}) - f(\mathcal{E}_{n\mathbf{k}})]$$
$$\times \frac{\langle m\mathbf{k}| v_x |n\mathbf{k}\rangle \langle n\mathbf{k}| v_y |m\mathbf{k}\rangle}{(\mathcal{E}_{m\mathbf{k}} - \mathcal{E}_{n\mathbf{k}})^2 + \eta^2}, \tag{9}$$

where m and n represent the band indices and $f(\mathcal{E}_{m(n)\mathbf{k}})$ is the Fermi-Dirac distribution function for energy $\mathcal{E}_{m(n)\mathbf{k}}$. $|m\mathbf{k}\rangle$ and $|n\mathbf{k}\rangle$ are eigenstates in $\mathbf{k}$-space corresponding to energies $\mathcal{E}_{m\mathbf{k}}$ and $\mathcal{E}_{n\mathbf{k}}$, respectively. $N = L_x \times L_y$ represents the size of the
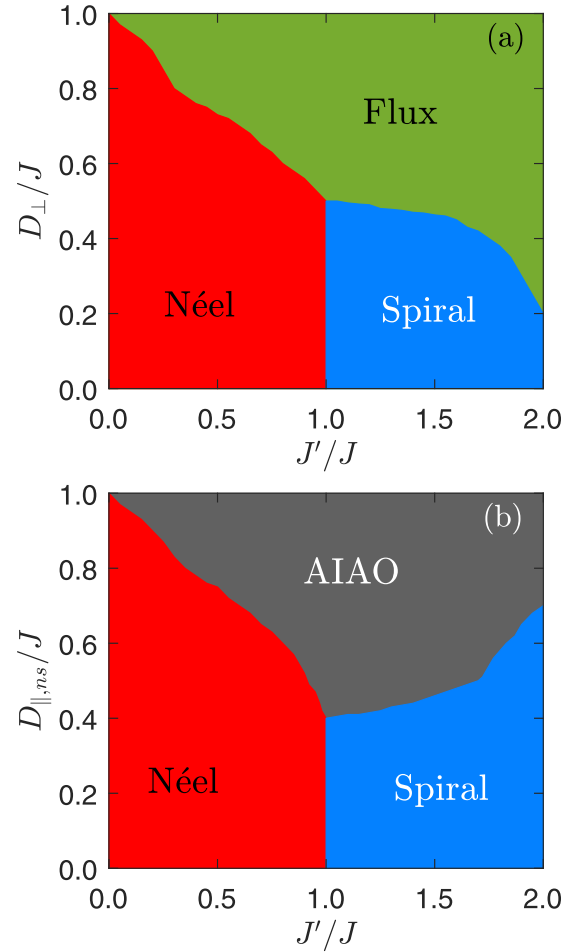
FIG. 2. Different magnetic ordered phases obtained in our simulation with varying J'/J and the DM vector components $D_\perp/J$ (a) and $D_{||,ns}/J$ (b). The other components of the DM vector D'/J or $D_{||,s}/J$ do not stabilize any additional new phases.

sample and η is the scattering rate. v_x and v_y are the velocity operators in k_x and k_y directions and can be expressed as

$$v_\mu = \frac{\partial \hat{\mathcal{H}}_e}{\partial k_{\hat{\mu}}}, \quad \mu = x, y. \tag{10}$$

For finite values of the Kondo coupling, we diagonalize Hamiltonian (2) for finite system sizes to obtain the energy spectrum of itinerant electrons moving on a background ordered phase. In this case, we calculate the transverse conductivity in $\mathbf{r}$-space as

$$\sigma_{xy} = \frac{ie^2\hbar}{N} \sum_{m,n\neq m} [f(\mathcal{E}_m) - f(\mathcal{E}_n)] \frac{\langle m| v_x |n\rangle \langle n| v_y |m\rangle}{(\mathcal{E}_m - \mathcal{E}_n)^2 + \eta^2},$$
$$\tag{11}$$

where $|m\rangle$, $|n\rangle$ are single-particle eigenstates corresponding to energies $\mathcal{E}_m$ and $\mathcal{E}_n$, and v_x and v_y are calculated as

$$v_\mu = \frac{i}{\hbar} \sum_{j,\sigma} (t_{j,j+\hat{\mu}} c^\dagger_{j,\sigma} c_{j+\hat{\mu},\sigma} - \text{H.c.}), \quad \mu = x, y. \tag{12}$$

In addition to the transverse charge conductivity, we also calculate the transverse spin conductivity, given by an analo-
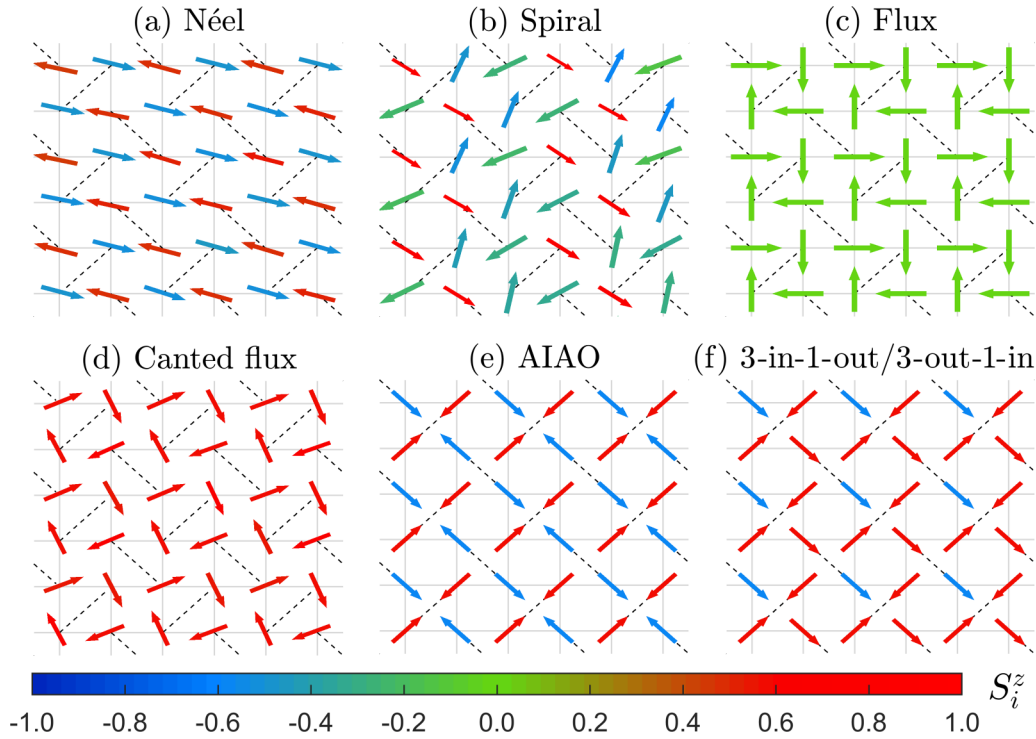
FIG. 3. The snapshots of real-space spin configurations of localized spins $\{\mathbf{S}_i\}$, for different magnetic ordered phases on the SS lattice as seen in our MC simulations. The xy components of spins are represented by arrows in the xy plane, while the z component is represented by the color scale. Hamiltonian parameters used to obtain the different phase are (a) Neél state at $J'/J = 0.8$, (b) spiral state at $J'/J = 2.0$, (c) flux state at $J'/J = 0.8$ and $D_\perp/J = 0.8$, (d) canted-flux state at $J'/J = 0.8$, $D_\perp/J = 0.8$, and $B/J = 5.2$, (e) AIAO state at $J'/J = 0.8$, $D_\perp/J = 0.8$, and $D_{\parallel,ns}/J = 0.7$, and (f) 3-in–1-out/3-out–1-in state at $J'/J = 0.8$, $D_\perp/J = 0.8$, $D_{\parallel,ns}/J = 0.2$, and $B/J = 4.0$.

gous Kubo formula that involves the spin current as

$$
\sigma_{xy}^S = \frac{ie}{4\pi N} \sum_{m,n\neq m} [f(\mathcal{E}_m) - f(\mathcal{E}_n)] \frac{\langle m| J_x |n\rangle \langle n| v_y |m\rangle}{(\mathcal{E}_m - \mathcal{E}_n)^2 + \eta^2},
$$

(13)

where $J_x = \frac{1}{2}\{v_x, \text{diag}(\mathbf{S}_1 \cdot \sigma, \dots, \mathbf{S}_N \cdot \sigma)\}$ is the spin current operator. As we shall discuss later, for $J_K \sim O(t)$, the spin Hall conductivity exhibits characteristic features very different from the charge Hall conductivity.

IV. RESULTS

A. Magnetic properties

Hamiltonian (1) exhibits a wide range of magnetic orderings in the ground state with varying parameters. We observe both collinear and noncollinear, coplanar and noncoplanar magnetic orderings for different sets of Hamiltonian parameters. The occurrence of a wide variety of ordered phases provides the motivation to study the motion of itinerant electrons on these backgrounds with the SS lattice geometry, thereby exploring the novel electronic properties on a SS lattice system.

We begin our study by tuning the frustration parameter J'/J, and different components of the DM vectors on the SS lattice (as shown in Fig. 1), in a systematic manner to identify the magnetic phase diagram in the parameter space spanned by J'/J and the parallel and perpendicular components of the DM vector. Figure 2 summarizes the results of our simula-

tions. In Fig. 3, we show the representative spin configurations of the principal ordered phases observed in our simulation in different parameter regimes.

In the absence of DM interaction, the ground state is a Néel antiferromagnet for $J'/J \leqslant 1$, and evolves to a spiral phase for $J'/J \gtrsim 1$ (Fig. 2). For this spiral phase, the angle difference between NN spins is $\theta = \pi \pm \cos^{-1}(J/J')$ for $J'/J > 1$ [43–45]. This can be understood as a consequence of the destabilization of the antiferromagnetic Néel state due to increasing frustration on the SS lattice. With the introduction of DM component $D_\perp/J$, there is a further competition to lower the energy of the spin configuration by perpendicular alignment of neighboring spins favored by the DM interaction term. Our results show that the spiral phase and the Néel phases are replaced by a coplanar "flux" phase with increasing $D_\perp/J$ [Fig. 2(a)] [46,47,50,51]. Upon the inclusion of $D_{\parallel,ns}/J$, a noncoplanar all-in/all-out (AIAO) phase is observed in the ground state for intermediate to strong values of $D_{\parallel,ns}/J$ [Fig. 2(b)]. The other components of the DM vector, D'/J or $D_{\parallel,s}/J$, do not stabilize any additional phases. The boundaries between the different phases can be obtained from the level crossing of the ground-state energy with the variation of the parameters in the Hamiltonian.

Next, we explore the effect of an external magnetic field on these ordered phases on the SS lattice. While it is tempting to map out the details of the evolution of all these candidate phases in the presence of an external magnetic field, we restrict ourselves to the regime $J'/J = 0.8$ (mainly due to the large parameter space of our model). The choice
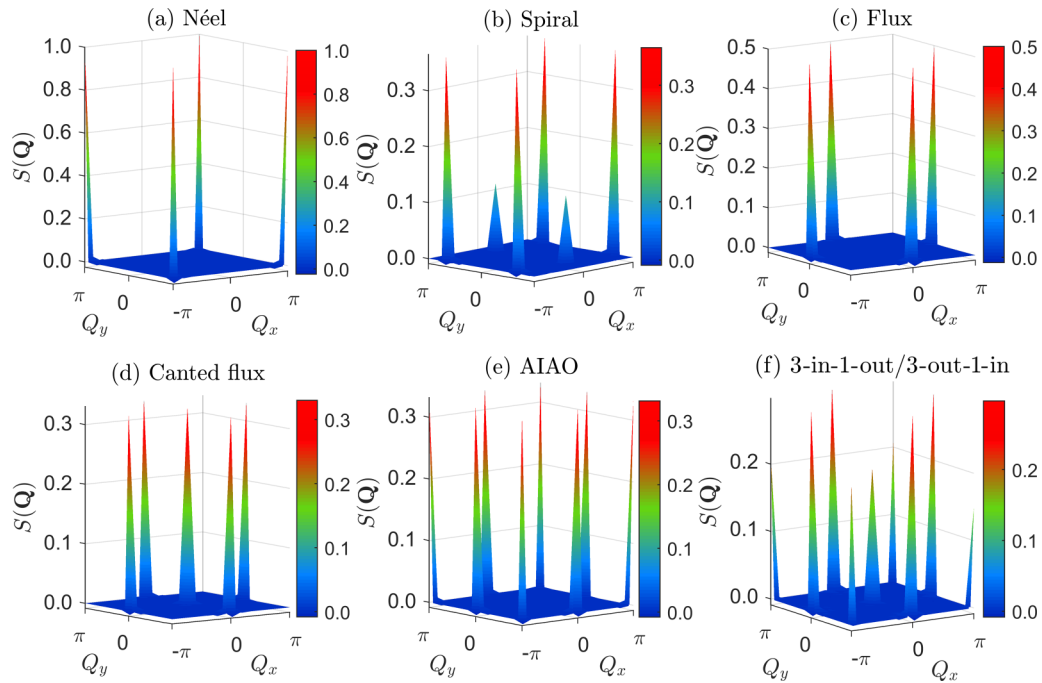
FIG. 4. Spin structure factor $S(\mathbf{Q})$ showing sharp peaks for different magnetic ordered phases on the SS lattice as shown in Fig 3. $S(\mathbf{Q})$ is calculated for $Q_x, Q_y \in [-\pi, \pi]$ and the weight is represented by the color scales. We characterize the ordered phases based on their peak locations. We observe $S(\mathbf{Q})$ peaks at (a) $\mathbf{Q} = (\pi, \pi)$ for the Néel state, (b) $\mathbf{Q} = (2\pi/3, 0)$ and $(2\pi/3, \pi)$ for the spiral phase, (c) $\mathbf{Q} = (0, \pi)$ and $(\pi, 0)$ for the flux phase, (d) $\mathbf{Q} = (0, 0)$, $(0, \pi)$, and $(\pi, 0)$ for the canted-flux phase, (e) $\mathbf{Q} = (0, \pi)$, $(\pi, 0)$, and (π, π) for the AIAO state, and (f) $\mathbf{Q} = (0, 0)$, $(0, \pi)$, $(\pi, 0)$, and (π, π) for the 3-in–1-out/3-out–1-in phase.

of this frustration parameter is motivated by experimental observation of nearly equal bond lengths in rare-earth compounds [37–39,52]. We characterize various ordered phases and study their evolution in the presence of an external magnetic field by focusing on observables such as spin structure factor and the scalar spin chirality.

Structure factor: A detailed understanding of the multiple magnetic states is provided by the magnetic structure factor, which quantifies the long-range magnetic order in terms of prominent peaks in the momentum space. In Fig. 4, we show the structure factor of different magnetic ordered phases observed in our simulation in different parameter regimes. We use the extended Brillouin zone (BZ) for the spin structure factor calculation. We can identify different ordered phases by the location and number of peaks observed in the spin structure factor. Since there is no spontaneous symmetry breaking in finite-size systems, we have examined the individual components of the structure factor $[\langle S_i^\mu S_j^\mu \rangle, \mu = x, y, z]$, and the real-space spin configuration obtained from the snapshots of the MC simulation to complement the total spin structure factor and to determine the multi-$\mathbf{Q}$ ordered phases. We observe the following features.

(i) In the absence of DM interaction and Zeeman field, the ground state shows an antiferromagnetic Néel ordering [see Fig. 3(a)]. This can be verified from Fig. 4(a) where the peak in spin structure factor appears at $\mathbf{Q} = (\pi, \pi)$. With increasing $D_\perp/J$, the ground state remains Néel antiferromagnet (AFM) until we reach a critical value $D_\perp^c/J \approx 0.62$, where we observe a phase transition marked by the sharp increase in the magnitude of the peak at $(0, \pi)$. The true nature of this ground state is revealed by the static spin structure factor

shown in Fig. 4(c), that exhibits two equal magnitude peaks at $\mathbf{Q} = (0, \pi)$ and $(\pi, 0)$ indicating a 2$\mathbf{Q}$ state. This is a noncollinear, coplanar flux state [see Fig. 3(c)]. Thus, the system undergoes a phase transition from 1$\mathbf{Q}$ phase (Néel state) to a 2$\mathbf{Q}$ phase (flux state) with increasing $D_\perp/J$.

(ii) Next, the evolution of the magnetic ordering for the flux state in the presence of an external magnetic field B/J is investigated for an illustrative value of $D_\perp/J$ (>0.62).[1] Introduction of a magnetic field leads to the canting of localized spins along the direction of B field [see Fig. 3(d)], for any nonzero B/J, which results in a 3$\mathbf{Q}$ magnetic ordering exhibiting three peaks (five peaks in the extended BZ) in $S(\mathbf{Q})$ at $\mathbf{Q} = (\pi, 0)$, $(0, \pi)$, and $(0,0)$. We designate this as the canted-flux state. In Fig. 5(a), we show the behavior of the structure factor peak at $\mathbf{Q} = (0, 0)$ as a function B/J for different values of $D_\perp/J$. It can be seen that $S(\mathbf{Q} = (0, 0))$ increases monotonically with increasing magnetic field strength. For very large B/J, the localized moments are aligned fully in the direction of B field, and ground state becomes a field polarized ferromagnetic state.

(iii) The introduction of the parallel components of DM vector either on axial or on diagonal bonds also results in the canting of localized spins. Figure 6 shows the effect of parallel component of DM vector on flux state. There is an

----

[1] A large $D_\perp/J$ is chosen as it amplifies the response of the magnetic field. While this is unrealistically large compared to the intrinsic DM strength in many real magnets, recent experiments have shown that a large DM interaction can be induced in magnetic thin films by forming interfaces with heavy metals.

additional peak in $S(\mathbf{Q})$ at (π, π) and its weight increases with the increase of strength of parallel component. Qualitatively, the effect is the same for all three parallel components of DM vectors, namely, $D_{\parallel,s}/J$, $D_{\parallel,ns}/J$, and D'/J. The ground state has 3**Q** magnetic ordering with peaks in $S(\mathbf{Q})$ at $\mathbf{Q} = (0, \pi)$, $(\pi, 0)$, and (π, π) as shown in Fig. 4(d). This phase corresponds to an AIAO state, where the orientation of four neighboring spins on the SS lattice plaquettes with diagonal bonds pointing in different directions can be mapped to the four radially inward and outward pointing vectors from the vertices of a regular tetrahedron [see Fig. 3(e)]. The transformation of the flux state to an AIAO state occurs for nonzero values of $D_{\parallel,ns}/J$ (or, alternatively, $D_{\parallel,s}/J$ or D'/J) that increases monotonically with $D_\perp/J$.

(iv) Next, we apply magnetic field in the presence of both in-plane and perpendicular components of DM vector. In the absence of magnetic field as mentioned in the previous paragraph, the magnetic ordering is that of an AIAO type. With the introduction of an external magnetic field, the localized moments reorient in the direction of the B field and we get an additional out-of-plane canting of these moments [see Fig. 3(f)]. The peak in spin structure factor at $\mathbf{Q} = (0, 0)$ grows with increasing magnetic field as shown in Fig. 7(a). The ground state now has 4**Q** ordering with peaks in $S(\mathbf{Q})$ located at $\mathbf{Q} = (0, 0)$, $(0, \pi)$, $(\pi, 0)$, and (π, π) as shown in Fig. 4(f). This is a 3-in–1-out/3-out–1-in state with three spins pointing in and one spin pointing out from the center of tetrahedron. Further increase in magnetic field results in all localized spins pointing in the direction of B field, a fully polarized ferromagnetic state.

Spin chirality: As seen above, multiple magnetic ordered phases are stabilized in the current model due to the interplay of the antiferromagnetic exchange interaction, the DM interaction, and the external magnetic field. To quantify the noncoplanarity of these spin textures we look into the scalar spin chirality χ [Eq. (8)]. Our calculation of χ gives the following results.

The Néel state being a collinear state has zero spin chirality. Further, the chirality also vanishes in the spiral phase. The chirality of flux state is zero as it is a 2**Q** noncollinear, but coplanar state. With increasing magnetic field on this flux state, the canting of the local moments in the direction of B field increases continuously until the local moments are fully polarized. The chirality for canted-flux state is nonzero as it is a noncoplanar state with 3**Q** magnetic ordering. As shown in Fig. 5(b), the chirality increases monotonically up to an intermediate value of the applied field and then decreases continuously to zero at saturation.

Introduction of any of the parallel components of DM vectors causes the flux state to have an out-of-plane canting of the localized spins. For such states, $S(\mathbf{Q})$ shows additional peaks at $\mathbf{Q} = (\pi, \pi)$. The weight of this peak increases with the increase of any of the in-plane components of DM vectors. This 3**Q** state is an AIAO state with nonzero spin chirality. Applying the magnetic field changes the AIAO state to a 3-in–1-out/3-out–1-in state. For this state, $S(\mathbf{Q})$ shows one more peak at $\mathbf{Q} = (0, 0)$. The enlarged out-of-plane component of the spins contributes to an increase in noncoplanarity of the ground state. The magnitude of the spin chirality increases with increasing magnetic field strength. The 3-in–1-out/3-
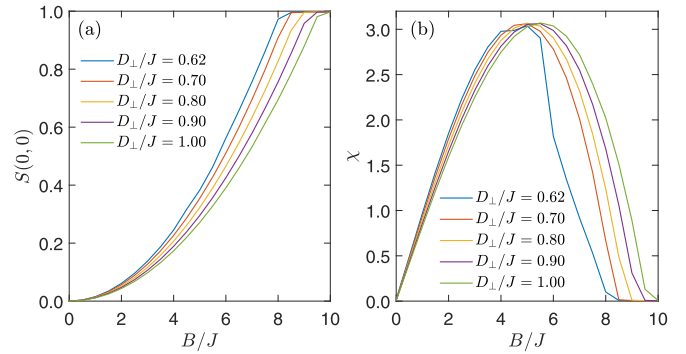
FIG. 5. (a) Variation of the structure factor peak height at $\mathbf{Q} = (0, 0)$ on the flux ground state with varying external magnetic field B/J for fixed values of DM vector component $D_\perp/J$. $S(0, 0)$ is finite for finite B/J values, and it increases monotonically with increasing B/J and eventually saturating for $B/J \sim 10$. (b) Behavior of the scalar spin chirality χ, with varying B/J for fixed values of $D_\perp/J$. $\chi = 0$ refers to a collinear/coplanar phase whereas $\chi \neq 0$ denotes a noncoplanar phase. χ increases rapidly with increasing B/J, reaching a maximum for $B/J \approx 5$, and then reduces gradually with further increase in B/J.

out–1-in state is a 4**Q** state with a nonzero chirality as shown in Fig. 7(b).

B. Electronic properties

Band structure: Coupling to the local moments modifies the transport properties of itinerant electrons dramatically. For simplicity, we consider a single band of s electrons interacting with the magnetic ordering via a Kondo coupling between the electron spin and the local moments, as given by the Hamiltonian (2). The dynamics of the electrons is fast compared to that of the localized classical spins. Consequently, at short timescales, the electrons effectively move in a static, but spatially varying magnetic field. Each local moment $\mathbf{S}_i$ acts as a local magnetic field whose action on the spin mag-
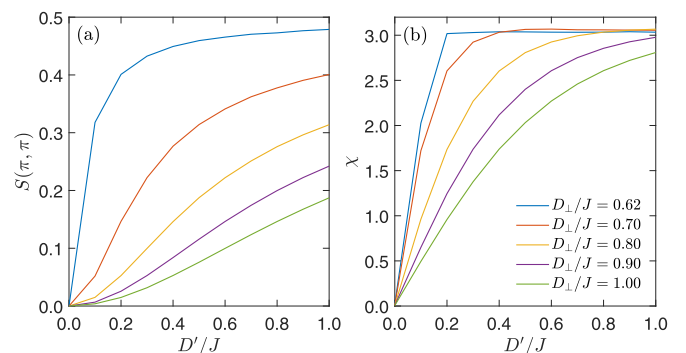
FIG. 6. Variation of $S(\mathbf{Q})$ peak height at $\mathbf{Q} = (\pi, \pi)$ as a function of DM vector component D'/J for fixed values of $D_\perp/J$. $S(\pi, \pi)$ increases monotonically with increasing D'/J values. The rise of $S(\pi, \pi)$ with D'/J is rapid for lower values of $D_\perp/J$ as compared to larger values of $D_\perp/J$. (b) Behavior of the scalar spin chirality χ at fixed $D_\perp/J$ with varying D'/J. χ increases monotonically with increasing D'/J. However, it rises rapidly and reaches the maximum quickly for lower values of $D_\perp/J$.
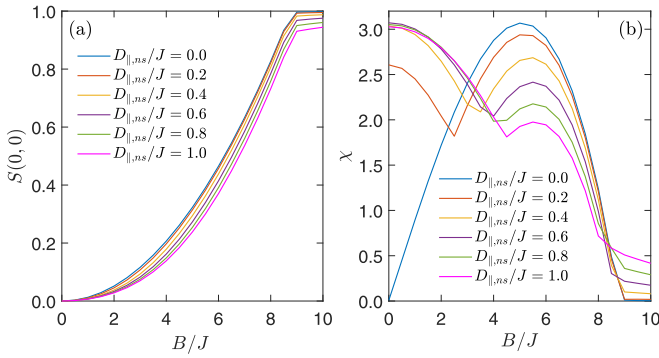
FIG. 7. (a) Behavior of the structure factor peak weight at $\mathbf{Q} = (0, 0)$ on the AIAO ground state as a function of external magnetic field B/J and the DM vector component $D_{\parallel,ns}/J$. $S(0, 0)$ is finite for finite B/J values, and it increases monotonically with increasing B/J and eventually saturating for $B/J \sim 10$. (b) Variation of scalar spin chirality with increasing B/J at fixed values of $D_{\parallel,ns}/J$. For $D_{\parallel,ns}/J = 0$, with increasing B/J, χ increases rapidly, reaches a maximum, and then reduces gradually reaching zero for $B/J \sim 10$. For $D_{\parallel,ns}/J \neq 0$, χ is finite in the $B/J = 0$ limit. χ shows a nonmonotonic behavior with increasing B/J and vanishes in the limit $B/J \approx 10$.

netic moment of the itinerant electrons $\mathbf{s}_i$ is described by a Kondo-type interaction $J_K \mathbf{S}_i \cdot \mathbf{s}_i$. In comparison, the Zeeman energy due the external magnetic field coupled to the spin of the electron is small and shall be neglected. In the following, the hopping amplitude along the axial bonds t is chosen to be unity ($t = 1.0$). For diagonal bonds the hopping matrix element is fixed at $t'/t = 0.8$.

In the absence of an external field, the electron band structure of SS lattice consists of four bands with twofold spin degeneracy as the SS lattice has four-site unit cell. One of the bands is flat along the diagonal of BZ which gives rise to strong van Hove singularity, where any interaction effects are maximized. A coupling to the spin texture increases the size of the unit cell in accordance with the periodicity of the magnetic ordering. The BZ is proportionately reduced and the bands are folded into the first BZ. $J_K > 0$ lifts the spin degeneracy and the energy bands for electrons with spins antiparallel and parallel to the local moments are shifted downward and upward, respectively. For sufficiently strong Kondo coupling, i.e., $J_K \gg t_{ij}$, the spin-parallel and -antiparallel bands are completely separated by a gap $2J_K$, and we end up with an effective tight-binding model as discussed in Sec. II. In this limit, the effective magnetic field produced by the spin texture couples directly to the charge degrees of freedom of the itinerant electrons, analogous to quantum Hall systems. The electron energy bands are modified depending on the nature of the underlying magnetic order.

In Fig. 8, we show the electronic band structure along a high-symmetry path in the first BZ, for the four magnetic ordered phases which are stabilized in the SS lattice. The high-symmetry points of BZ taken in the calculations are $\Gamma = (0, 0)$, $M = (\pi/2, 0)$, and $K = (\pi/2, \pi/2)$. We observe the following key features.

(i) *Flux state:* The magnetic unit cell of the SS lattice remains as four sites for flux-type ordering of the localized spins. The band structure consists of eight bands and for
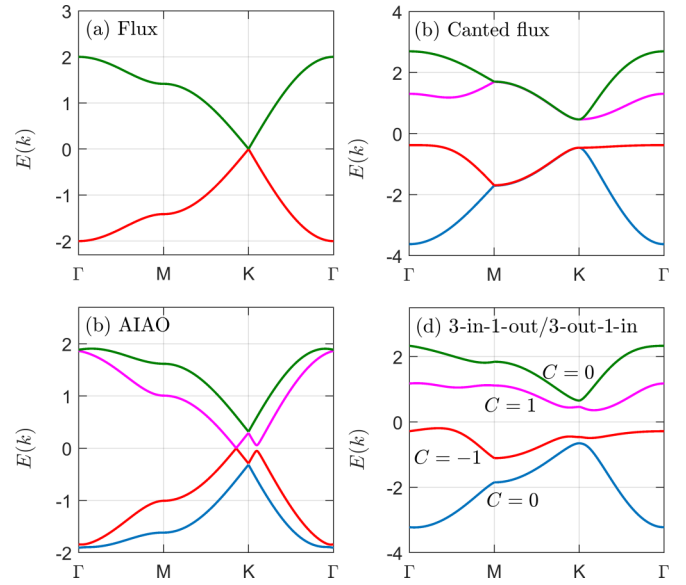
FIG. 8. The band structure for itinerant electrons plotted along a high-symmetric path in the BZ for different magnetic orderings of localized spins: (a) flux state, (b) canted-flux state, (c) AIAO state, and (d) 3-in–1-out/3-out–1-in state. The ratio of hopping matrix on diagonal and axial bond is set to $t'/t = 0.8$.

large J_K these split into four bands each for spin-parallel and -antiparallel alignment of itinerant electrons with the localized moments. We show the dispersion of itinerant electrons when they move on the background of flux phase in Fig. 8(a). The four spin-anti-parallel bands are doubly degenerate and touch each other at the K point of BZ.

(ii) *Canted-flux state:* For this magnetic state, the dispersion of conduction electrons is plotted in Fig. 8(b). It consists of four bands with degeneracy of the bands partially lifted. There is a gap opening between the upper and lower pair of bands. The noncoplanar canted-flux state not only lifts the degeneracy, but also opens up a direct band gap at the K point.

(iii) *AIAO state:* For this state, the magnetic unit cell is also four sites. The band structure comprises of four bands as shown in Fig. 8(c). The degeneracy of the bands is lifted and we observe an indirect gap between upper and lower pair of bands at the K point. Interestingly, the middle two bands touch each other at a point close to the K point.

(iv) *3-in–1-out/3-out–1-in state:* The size of the magnetic unit cell remains same as the SS lattice for this magnetic ordering. The degeneracy of all four bands is fully lifted and we observe direct as well as indirect band gaps between the bands as shown in Fig. 8(d). We calculate the Chern number of the bands in this state and found that two bands have nonzero Chern numbers [see Fig. 8(d)].

Hall conductivity at infinite Kondo coupling: The coupling to local moments modifies the transport properties of itinerant electrons significantly in metallic magnets. The effect is most dramatic in the transverse conductivity, especially when the underlying spin arrangement is noncoplanar. In a magnetic metal, the Hall resistivity consists of three contributions,

$$\rho_{xy} = \rho_{xy}^{\text{NHE}} + \rho_{xy}^{\text{AHE}} + \rho_{xy}^{\text{THE}},$$
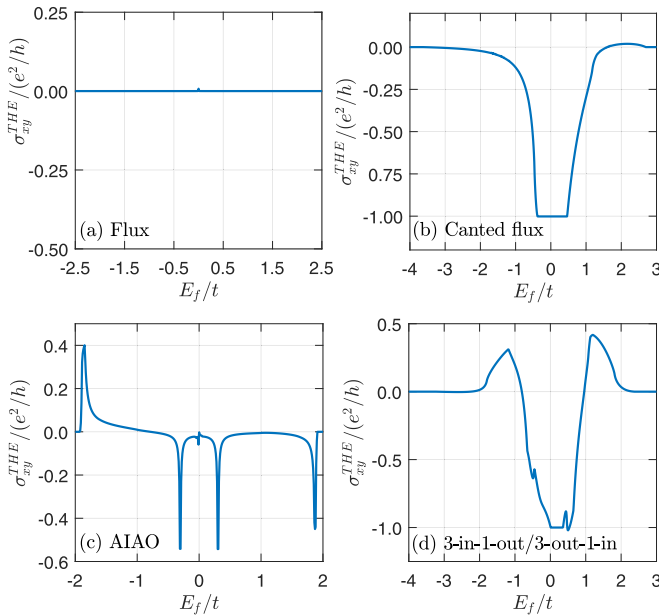
FIG. 9. Topological Hall conductivity of conduction electrons in the $J_K \gg t$ limit, as a function of Fermi energy, when they move in the background of different magnetic phases: (a) flux state, (b) canted-flux state, (c) AIAO state, and (d) 3-in–1-out/3-out–1-in state. We use $t'/t = 0.8$.

where NHE, AHE, and THE refer to normal, anomalous, and topological Hall effects, respectively. The AHE appears in metals with a net magnetization due to spin-orbit coupling. On the other hand, THE arises due to the Berry phase acquired by an electron moving in a noncoplanar spin texture. The phenomenon is best understood within the framework of the effective Hamiltonian (3) in the strong coupling limit ($J_K \gg t$). In this limit, the Berry phase acquired by an electron moving around a closed plaquette results in an effective flux threading each such plaquette that acts as a fictitious magnetic field and gives rise to a Hall effect, whose origin is purely geometrical. Further, it depends on the value of the Fermi energy. In this work, we focus only on the contribution of THE to the transverse conductivity for different background magnetic phases with varying Fermi energy. In the strong coupling limit, we use the Hamiltonian (3) and the momentum space Kubo formalism [Eq. (9)] to study the THE. We observe the following.

(i) *Flux state:* The Hall conductivity of electrons moving on a background of the flux phase with the electron spin strongly coupled to the local moment is plotted in Fig. 9(a) for varying the chemical potential values. We observe the Hall conductivity remains zero throughout the entire range of chemical potential. As identified earlier, the flux state is a coplanar state with zero chirality. This explains the vanishing THE for the flux state.

(ii) *Canted-flux state:* As discussed before, the canted-flux state is a 3**Q** state and the electronic band structure displays a direct band gap at the K point for this state. Further, the spin chirality associated with this noncoplanar state is nonzero, and that contributes to THE. The transverse conductivity as a function of Fermi energy for canted-flux state is shown in

Fig. 9(b). We observe a plateau in the Hall conductivity as the chemical potential falls in the band gap. The Hall conductivity has the quantized value -1 (in units of e^2/h).

(iii) *AIAO state:* The behavior of Hall conductivity with changing chemical potential for this phase is shown in Fig. 9(c). There is a nonzero value of Hall conductivity for small range of Fermi energy which is attributed to nonzero value of chirality for this state. The value of the conductivity is not an integer as there is no direct band gap between the energy bands.

(iv) *3-in–1-out/3-out–1-in state:* The most interesting outcome of our work is observed for this magnetic state. This magnetic phase is noncoplanar with nonzero value of chirality. We also observe that degeneracy of all the bands is fully lifted and there are direct and indirect gaps between the bands. The Hall conductivity for this phase is shown in Fig. 9(d) and it remains nonzero for a large window of Fermi energy lying between $-2t$ and $2t$. Again, the noncoplanarity of this phase manifests itself through nonzero value of THE. When the gap between the energy bands is direct, the quantized Hall conductivity remains -1 (in units of e^2/h) for the width of band gap. The quantized value of σ_{xy} is related to the sum of Chern numbers of the lowest two bands in the energy spectrum [see Fig. 8(d)]. This is a signature of integer THE similar to integer quantum Hall effect observed in quantum Hall systems.

Hall conductivity at finite Kondo coupling: Having studied the behavior of the topological Hall effect in the ground state in the $J_K \gg t$ limit, we next attempt to find it at intermediate values of the Kondo coupling $J_K \sim O(t)$. We use the Hamiltonian (2) and the real-space Kubo formalism [Eq. (11)] to perform our transport calculations in this regime. Unlike the $J_K \gg t$ limit, where the contribution to the Hall conductivity is due to the electronic states of either the spin antiparallel or the spin parallel to the local moments, for $J_K \sim O(t)$, the contribution is due to the electronic states of both spin parallel and antiparallel to the local moments. In addition, we also consider the contribution of spin-flip hopping terms due to the noncoplanar orderings of localized spins. Further, the contribution to topological Hall effect strongly depends on the value of Fermi energy.

We calculate the Hall conductivity for a canted-flux state and a 3-in–1-out/3-out–1-in state for finite Kondo coupling values by varying the Fermi energy. The results are shown in Fig. 10. We observe that for both the spin backgrounds (i) the Hall conductivity due to the electrons aligned antiparallel and parallel show similar contribution, but with opposite signs for $J_K = 8t$. This can be understood by the fact that the opposite electron spin alignment with respect to the local magnetic ordered phases gives rise to emergent magnetic fields of opposite signs. As a manifestation of this effect, in a semiclassical picture, electrons of opposite spins deflect in opposite transverse directions due to the emergent magnetic fields. σ_{xy} changes sign as the Fermi energy crosses a van Hove singularity. It exhibits a quantized value when the Fermi energy lies within the band gap for both the ordered phases. (ii) For $J_K = t$, the Hall conductivity not only shows distinct features as compared to the $J_K \gg t$ limit, but also has a large contribution even at $E_f = 0$. This contribution to the Hall conductivity is due to the overlap of the electronic states aligned parallel and antiparallel to the local spin background.
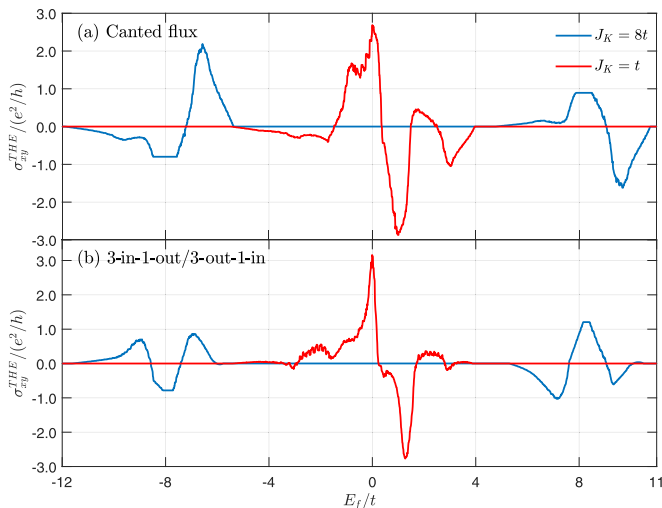
FIG. 10. Behavior of topological Hall conductivity as a function of the Fermi energy for $J_K = 8t$ and t, with conduction electrons coupled to (a) canted-flux state and (b) 3-in–1-out/3-out–1-in state orderings of the localized moments on the SS lattice.

FIG. 11. Behavior of topological spin Hall conductivity as a function of the Fermi energy for different Kondo coupling values of conduction electrons coupled to (a) canted-flux state and (b) 3-in–1-out/3-out–1-in state orderings of the localized moments.

Here, as in the previous case, σ_{xy} changes sign as the Fermi energy crosses a van Hove singularity. However, σ_{xy} does not show any quantized values over the whole range of Fermi energy, indicating the absence of any clear band gap in the electronic states. We would like to emphasize that with the increase of J_K the contribution from spin-flip hopping terms becomes smaller and for very large Kondo coupling ($J_K \gg t$) this contribution is zero and we reproduce results similar to Fig. 9. However, if we do not consider the spin-flip hopping terms then for $J_K \geqslant 5t$ the transverse conductivity results match with that of infinite Kondo coupling.

Next, we discuss the behavior of the topological spin Hall conductivity (σ_{xy}^S). While both σ_{xy} and σ_{xy}^S are interlinked, they also exhibit some distinct features which makes this study interesting. Figure 11 shows the variation of the spin Hall conductivity with changing chemical potential for different values of J_K on the canted-flux and the 3-in–1-out/3-out–1-in phases, respectively. In the strong coupling limit ($J_K \gg t$), the energy bands for local spin-aligned and -antialigned electrons are separated by a wide band gap. As a result, σ_{xy} and σ_{xy}^S follow one another closely. In this limit, only one species of electrons contributes to the Hall conductivities. Both σ_{xy} and σ_{xy}^S, exhibit sharp jumps and change signs as the Fermi energy is tuned across the van Hove singularities. For $J_K \sim t$, the local spin polarization is incomplete. This leads to different fractions of spin-parallel and spin-antiparallel states with strong overlap in energy of these states. The electron spin states hybridize and the spins of itinerant electrons are not simply aligned or antialigned to the local moments. The energy eigenstates have contributions from both electronic spin states. As a consequence, the σ_{xy} and σ_{xy}^S are decoupled from
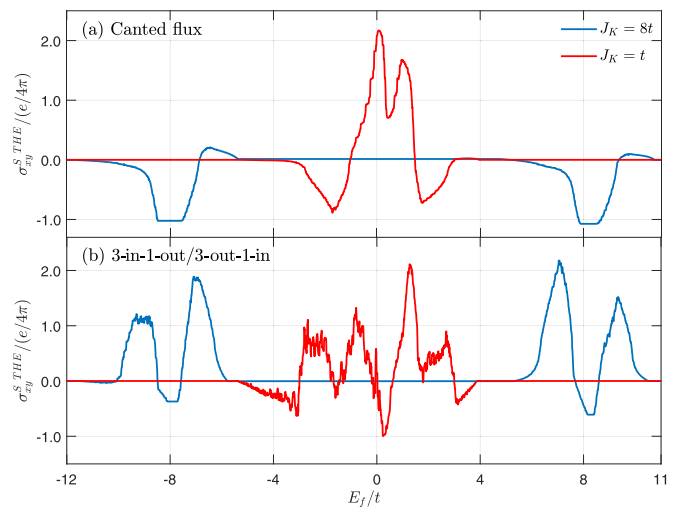
each other. For $J_K = t$, there exist ranges of Fermi energy for which $\sigma_{xy}^S > \sigma_{xy}$. This is suggestive of the fact that electrons with opposite spins are deflected in opposite directions, which leads to an increase in the spin Hall conductivity and a decrease in the charge Hall conductivity as compared to the case of the zero-field nonoverlapping band scenario.

V. SUMMARY

We have identified multiple noncollinear and noncoplanar magnetic phases stabilized on the SS lattice in the presence of competing antiferromagnetic exchange couplings, DM interaction, and an external magnetic field. We discuss the role of in-plane and out-of-plane components of the DM vectors, and external magnetic field in the stabilization of these exotic ground states of localized moments. Having identified the unconventional magnetic orderings, we discuss the electronic properties due to the coupling of itinerant electrons to these complex spin textures, focusing on the topological Hall effect. Our study of THE on SS lattice for strong and intermediate Kondo couplings between localized spins and itinerant electrons shows distinct contributions to Hall conductivities. Our results predict occurrence of THE on SS lattice and may be seen in experiments on rare-earth tetraborides.

[1] E. Dagotto, T. Hotta, and A. Moreo, Phys. Rep. **344**, 1 (2001).

[2] C. Buhler, S. Yunoki, and A. Moreo, Phys. Rev. Lett. **84**, 2690 (2000).

[3] R. Ozawa, S. Hayami, K. Barros, G.-W. Chern, Y. Motome, and C. D. Batista, J. Phys. Soc. Jpn. **85**, 103703 (2016).

[4] S. Reja, R. Ray, J. van den Brink, and S. Kumar, Phys. Rev. B **91**, 140403(R) (2015).

[5] C. Zener, Phys. Rev. **82**, 403 (1951).

[6] P. W. Anderson and H. Hasegawa, Phys. Rev. **100**, 675 (1955).

[7] N. Furukawa, J. Phys. Soc. Jpn. **64**, 2734 (1995).

[8] S. Yunoki, J. Hu, A. L. Malvezzi, A. Moreo, N. Furukawa, and E. Dagotto, Phys. Rev. Lett. **80**, 845 (1998).

[9] K. Kubo and N. Ohata, J. Phys. Soc. Jpn. **33**, 21 (1972).

[10] G.-W. Chern, SPIN **05**, 1540006 (2015).

[11] D. Grohol, K. Matan, J.-H. Cho, S.-H. Lee, J. W. Lynn, D. G. Nocera, and Y. S. Lee, Nat. Mater. **4**, 323 (2005).

[12] I. Martin and C. D. Batista, Phys. Rev. Lett. **101**, 156402 (2008).

[13] S. Hayami and Y. Motome, Phys. Rev. B **91**, 075104 (2015).

[14] Y. Taguchi, Y. Oohara, H. Yoshizawa, N. Nagaosa, and Y. Tokura, Science **291**, 2573 (2001).

[15] G.-W. Chern and C. D. Batista, Phys. Rev. Lett. **107**, 186403 (2011).

[16] Y. Akagi and Y. Motome, Phys. Rev. B **91**, 155132 (2015).

[17] S. Reja, J. van den Brink, and S. Kumar, Phys. Rev. B **93**, 155115 (2016).

[18] H. Ishizuka and Y. Motome, Phys. Rev. B **88**, 081105(R) (2013).

[19] S. Kumar and J. van den Brink, Phys. Rev. Lett. **105**, 216405 (2010).

[20] S. Hayami, T. Misawa, Y. Yamaji, and Y. Motome, Phys. Rev. B **89**, 085124 (2014).

[21] S. Ghosh, P. O'Brien, C. L. Henley, and M. J. Lawler, Phys. Rev. B **93**, 024401 (2016).

[22] R. Karplus and J. M. Luttinger, Phys. Rev. **95**, 1154 (1954).

[23] J. Ye, Y. B. Kim, A. J. Millis, B. I. Shraiman, P. Majumdar, and Z. Tešanović, Phys. Rev. Lett. **83**, 3737 (1999).

[24] D. Xiao, M.-C. Chang, and Q. Niu, Rev. Mod. Phys. **82**, 1959 (2010).

[25] S. Yoshii, S. Iikubo, T. Kageyama, K. Oda, K. Kondo, K. Murata, and M. Sato, J. Phys. Soc. Jpn. **69**, 3777 (2000).

[26] Y. Machida, S. Nakatsuji, Y. Maeno, T. Tayama, T. Sakakibara, and S. Onoda, Phys. Rev. Lett. **98**, 057203 (2007).

[27] M. Udagawa and R. Moessner, Phys. Rev. Lett. **111**, 036602 (2013).

[28] Y. Kato, I. Martin, and C. D. Batista, Phys. Rev. Lett. **105**, 266405 (2010).

[29] K. Barros and Y. Kato, Phys. Rev. B **88**, 235101 (2013).

[30] K. Ohgushi, S. Murakami, and N. Nagaosa, Phys. Rev. B **62**, R6065 (2000).

[31] K. Barros, J. W. F. Venderbos, G.-W. Chern, and C. D. Batista, Phys. Rev. B **90**, 245119 (2014).

[32] G.-W. Chern, A. Rahmani, I. Martin, and C. D. Batista, Phys. Rev. B **90**, 241102(R) (2014).

[33] H. D. Rosales, F. A. Gómez Albarracín, and P. Pujol, Phys. Rev. B **99**, 035163 (2019).

[34] G.-W. Chern, Phys. Rev. Lett. **105**, 226403 (2010).

[35] R. Shindou and N. Nagaosa, Phys. Rev. Lett. **87**, 116801 (2001).

[36] J. W. F. Venderbos, M. Daghofer, J. van den Brink, and S. Kumar, Phys. Rev. Lett. **109**, 166405 (2012).

[37] S. S. Sunku, T. Kong, T. Ito, P. C. Canfield, B. S. Shastry, P. Sengupta, and C. Panagopoulos, Phys. Rev. B **93**, 174408 (2016).

[38] K. Siemensmeyer, E. Wulf, H.-J. Mikeska, K. Flachbart, S. Gabáni, S. Mat'aš, P. Priputen, A. Efdokimova, and N. Shitsevalova, Phys. Rev. Lett. **101**, 177201 (2008).

[39] K. Wierschem, S. S. Sunku, T. Kong, T. Ito, P. C. Canfield, C. Panagopoulos, and P. Sengupta, Phys. Rev. B **92**, 214433 (2015).

[40] T. Suzuki, Y. Tomita, N. Kawashima, and P. Sengupta, Phys. Rev. B **82**, 214404 (2010).

[41] F. Iga, A. Shigekawa, Y. Hasegawa, S. Michimura, T. Takabatake, S. Yoshii, T. Yamamoto, M. Hagiwara, and K. Kindo, J. Magn. Magn. Mater. **310**, e443 (2007).

[42] S. Michimura, A. Shigekawa, F. Iga, T. Takabatake, and K. Ohoyama, J. Phys. Soc. Jpn. **78**, 024707 (2009).

[43] A. Grechnev, Phys. Rev. B **87**, 144419 (2013).

[44] M. Moliner, D. C. Cabra, A. Honecker, P. Pujol, and F. Stauffer, Phys. Rev. B **79**, 144401 (2009).

[45] B. S. Shastry and B. Sutherland, Phys. B+C (Amsterdam) **108**, 1069 (1981).

[46] M. Shahzad and P. Sengupta, Phys. Rev. B **96**, 224401 (2017).

[47] M. Shahzad and P. Sengupta, Phys. Rev. B **96**, 224402 (2017).

[48] M. Shahzad and P. Sengupta, J. Phys.: Condens. Matter **29**, 305802 (2017).

[49] N. Nagaosa, J. Sinova, S. Onoda, A. H. MacDonald, and N. P. Ong, Rev. Mod. Phys. **82**, 1539 (2010).

[50] M. Yamanaka, W. Koshibae, and S. Maekawa, Phys. Rev. Lett. **81**, 5604 (1998).

[51] D. F. Agterberg and S. Yunoki, Phys. Rev. B **62**, 13816 (2000).

[52] L. Ye, T. Suzuki and J. G. Checkelsky, Phys. Rev. B **95**, 174405 (2017).